

Supplementary Materials for
Embodying soft robots with octopus-inspired hierarchical suction intelligence

Tianqi Yue *et al.*

Corresponding author: Jonathan Rossiter, jonathan.rossiter@bristol.ac.uk

Sci. Robot. **10**, eadr4264 (2025)
DOI: 10.1126/scirobotics.adr4264

The PDF file includes:

Supplementary Methods
Figs. S1 to S17
Tables S1 to S3
Legends for movies S1 to S8

Other Supplementary Material for this manuscript includes the following:

Movies S1 to S8

Theoretical Derivation of Suction Flow-Based Multimodal Perception

The physical model of experimental setup is shown in fig. S3. For Case 1, the thin silicone tube from the suction cup's central hole to the pressure sensor's connection site dominates the pressure drop. For Case 2, the thin aperture of the sealing region, rather than the thin tube of Case 1, dominates the pressure reduction. Note that, Case 2 only considers surfaces not too rough (based on our experiments, sandpaper ≥ 400 grits), otherwise the aperture will be too large and no difference will be measured with respect to Case 1. Regarding the two cases, p_m is governed by (33)

$$\begin{aligned} p_{m, \text{case } 1} &= -\frac{128\mu Q L_1}{\pi d^4} \\ p_{m, \text{case } 2} &= -\frac{12\mu Q L_x}{L_y t^3} \end{aligned} \quad (1)$$

where μ is the dynamic viscosity of the fluid, Q is the suction flow rate, L_1 and $d = 0.4$ mm are the length and inner diameter of the tube as denoted in fig. S3, L_x and L_y are geometric parameters of the sealing region, and t is the mean aperture size in the sealing region. Note that L_1 , d and L_x/L_y are constant when the sucking and leaking are dynamically balanced (33). Therefore,

$$\begin{aligned} p_{m, \text{case } 1} &= f(\mu, Q) \\ p_{m, \text{case } 2} &= f(\mu, Q, t). \end{aligned} \quad (2)$$

The diaphragm pump used in the experiments is driven by a DC motor. Therefore,

$$V = E + IR_{DC}, \quad (3)$$

where $V = 3$ V is the constant voltage powering the pump, I is the current used to actuate the DC motor, R_{DC} is the electric resistance of the motor's coil and E is the back electromotive force (EMF) generated during pumping. $E = K_b \omega$, where K_b is the back EMF constant and ω is the rotational speed of DC motor's shaft. For a diaphragm pump, $\omega = K_f Q$, where K_f is the ratio of motor's rotational speed to flow rate. The resistant torque of the DC motor is proportional to the current, $T = K_t I$, where K_t is the torque sensitivity. Meanwhile, $T = K_p(p_{out} - p_{in}) = K_p(p_e - p_{in})$, where $(p_{out} - p_{in})$ is the pumping-generated pressure differential between the outlet and the inlet, and K_p is the ratio of this pressure differential to the resistant torque.

For Case 1 (a laminar flow in the tube), the below relation can be derived:

$$\frac{p_{in} - p_s}{p_s - p_e} = \frac{p_{in} - p_s}{p_m} = \frac{L_2}{L_1}. \quad (4)$$

Substituting all equations above into Equation (3), we then obtain

$$Q = \frac{K_p R_{DC}(L_1 + L_2)}{K_b K_f K_t L_1} p_m + \frac{V}{K_b K_f} = f(p_m), \quad (5)$$

indicating that flow rate Q is a function of p_m in the given experimental conditions, that is, $Q = f(p_m)$.

For Case 2 (leakage in the sealed region), the suction gap t is a function of three parameters (34): Young's modulus of the suction disc E , roughness of the contacting surface R and the contacting pressure p_{contact} . p_{contact} is expressed as

$$p_{\text{contact}} \approx \frac{F_{\text{bend}}}{A_{\text{contact}}} + \beta(p_e - p_m), \quad (6)$$

where F_{bend} is the bending-induced force, A_{contact} is the area of the ring-shaped sealing stripe, β is a scalar between 0.5 and 1, depending on the pressure distribution in the sealing stripe. F_{bend} depends on the geometrical deformation of the suction disc, which is dependent on F_{pull} . Combining the above conditions, suction gap t is dependent on p_m , R and F_{pull} , that is, $t = f(p_m, R, F_{\text{pull}})$.

Substituting $Q = f(p_m)$ and $t = f(p_m, R, F_{\text{pull}})$ into Equation (2), p_m is a function of three environment-related variables – viscosity, roughness and pulling force,

$$\begin{aligned} p_{m, \text{case 1}} &= f_1(\mu) \\ p_{m, \text{case 2}} &= f_2(\mu, R, F_{\text{pull}}). \end{aligned} \quad (7)$$

Details of the Experimental Setups for Demonstrating the Suction-Based Embodied Intelligence

We demonstrated lower-level suction-based embodied intelligence through three experiments:

In the first experiment, the gentle-touch robotic finger and robotic hand (Fig. 2C-D): Details of the experimental setup are provided in fig. S1. In this experiment, a desktop robotic arm (MG400, Dobot) carried the finger (or hand) vertically, positioning it at the appropriate locations. The actuator (that is, the fluidic chamber) was connected to the OUT port of the diaphragm pump, while the sucker was attached to the IN port. The pump was manually controlled via a 3 V DC power source, switching it on and off as required.

In the second experiment, the sequential grasping robotic hand and octopus-like arm (Fig. 3): Details of the experimental setup are shown in fig. S2. In this case, the ends of the hand and the arm were mounted onto the robotic arm (MG400, Dobot). Multiple identical pumps, as used in the gentle-touch finger experiment, and multiple suction-triggered switches (STSs) were employed, connected in the configuration illustrated in Fig. 2F. The pumps were similarly manually operated using a 3 V DC power source. Notably, in Fig. 3D and E, we demonstrated a compact intelligent hand by integrating pumps, smaller STSs, a 3.7 V lithium battery (EEMB 542730, in place of a benchtop power supply) and an on-off switch. The smaller STSs, as shown in Fig. 3D, had dimensions reduced to half those of the original larger STS (dimensions in fig. S14), resulting in 1/8 volume (87.5% reduction) of the original.

In the third experiment, the integrated embodied control and sensing soft gripper (Fig. 5): Details of the experimental setup are provided in fig. S6. The same pumps and STSs were used as in the previous experiments. The target object featured a rough top surface made of sandpaper with varying grades of roughness. Additional weights, comprising one or two 100 g masses, were employed to vary the object's overall weight.

The system mainly consisted of following parts: pumps, actuators, suction cups, STSs and tubes. Some aspects should be taken into consideration:

There were no strict requirements for the design of suction cups. Dimensions of the suction cups used in this study are shown in fig. S14A and B. All suction cups were made by casting Dragon Skin 10 NV. It should be noted that the mould generating the bottom side of the suction cup needs to be smooth enough. Our approach was to use 3D printed Acrylonitrile Butadiene Styrene (ABS) moulds, then we sprayed acetone to remove the layer textures and finally polished the surface by sandpapers smoother than 3000 grit.

The pumps utilised in this study were commercially available small diaphragm pumps, with a rated voltage of 3 V and a maximum current of 190 mA. The pump's dimensions are provided in fig. S15A. These pumps are designed for safe long-term operation, even when their ports are blocked by the suction cups and the STSs. To evaluate this, we selected two pumps and measured their current under both no-load (all ports open) and blocked conditions (all ports closed). Slight variations in performance may occur due to manufacturing tolerances. However, the results, presented in fig. S15B, indicate that both pumps operate well under blockage. Furthermore, the current fluctuations consistently remained within the safe operating range (< 190 mA).

Another consideration was that the pumps must provide sufficient negative pressure to achieve suction adhesion even when the actuator was highly inflated. The diaphragm pump generated a constant pressure

differential under a constant voltage supply. In other words, the sum of the negative suction pressure (at the IN port) and the positive inflation pressure (at the OUT port) remained constant. This was demonstrated in the gentle grasping experiment using the finger (Fig. 2C), as shown in fig. S16. When the finger was inflated to 44.5 kPa, which is near the pump's upper limit, the suction cup still successfully generated adhesion. However, the suction pressure under this condition was consequently lower compared to when the finger was not highly inflated, indicating a weaker adhesion and might cause the STS failed to be triggered.

Due to the need for independent control of multiple segments in our embodiments, the number of tubes increased linearly with number of segments. We intentionally left the tubes relatively long to ensure sufficient length for reconfiguring the STSs and motors, and manually arranged the tubes to prevent interference with chamber movement. Future work will consider embedding tubes inside the chamber, such as reported in (42).

Actuators in this study were made by casting silicone (Dragon Skin 10 NV, Smooth-on). The inextensible layer was made by embedding the non-woven fabric into a 1-mm layer of Dragon Skin 10 NV. The safety of the actuator should be considered, especially when the suction cup did not establish the seal and then the pump continuously pumps air into the actuator. When the pump was powered by 3 V, the measured pressure output is shown in fig. S17A. When the IN port of the pump was open, the maximum inflating pressure from the OUT port reached 55.7 kPa. Conversely, when the OUT port was open, the maximum suction pressure from the IN port was -37.9 kPa. Although there may be slight variations in pressure among individual pumps due to manufacturing errors, this pressure range remained well within safe limits for Dragon Skin 10 NV, which had a tensile strength of 2.8 MPa. An example highly inflated actuator is shown in fig. S17B. This implies the safety of the system even in the worst condition. Likewise, the material properties prevented damage to the suction cup as well.

Since the STS required negative pressure to be triggered (utilising suction pressure), careful consideration of the triggering pressure was essential. The original, larger STS (featuring a snapping membrane made from Dragon Skin 10 NV) had a triggering pressure range of -6 to -9 kPa (subject to manufacturing error), making it easily triggered. However, scaling down the STS to half its original size increased the triggering pressure to -30 to -33 kPa. To ensure successful triggering of the smaller STS when the actuator is inflated, EcoFlex 00-50 was employed for fabricating the snapping membrane as shown in Fig. 3D, reducing the triggering pressure to a range of -16 to -19 kPa. In summary, the snapping stiffness must be carefully designed to align with the pump's characteristics, which can be achieved by adjusting the materials and geometries of the snapping membrane.

Details for Suction-Based Multimodal Perception

Data partition

Raw data was collected from the experiments detailed in the main text. We first manually partitioned all the raw data according to different events shown in Fig. 4 and table S1, then labelled them. 90% of the raw labelled data were randomly selected to generate the training data sets, while the remaining 10% of the raw labelled signals were used to generate the testing data set, ensuring no overlap between the two.

Features of collected raw data

We observed that the pressure signal has a step change after the suction cup contacts a dry surface (as shown in the examples in fig. S4A), which stabilises after about 20 consecutive data points (~ 0.44 s). In the case of underwater contact (as shown in the examples in fig. S4B), the step change gradually stabilises after about 140 consecutive data points (~ 3.06 s). When the suction cup transitions between air and water (as shown in the examples in fig. S4C), the pressure signal also changes rapidly within 20 consecutive data points (although the stabilisation might take a longer time). The duration of these three events is as shown in fig. S4D.

Data slicing

From the raw data we can see that the pressure signal response is much faster in air than in water. This is caused by the viscosity difference between the two mediums as we analysed in the main text. 20 consecutive data points (~ 0.44 s) can be used for the air models (M_1 and M_2) to include enough information within this duration, while 140 consecutive data points (~ 3.06 s) can be used for the water models (M_3 and M_4). Therefore, we use the shorter and longer sliding windows to slice the raw labelled training and testing data, thereby the training and testing data sets can be obtained, as shown in fig. S4E.

Data training

We used the built-in fine decision tree model in MATLAB with default settings to train the datasets. As shown in fig. S4F to I, M_1 , M_2 and M_3 show high accuracy with mean $> 95\%$, while only M_4 has a lower accuracy with mean $\sim 71\%$. This is caused by the discontinuity when transitioning between different mediums, which has been discussed in the main text.

For the soft gripper with hierarchical intelligence

We use the same method as the suction-based sensing. The window size is 140 data points (~ 3.06 s), considering that water was involved in the experiment which may delay the response. In our design (Fig. 5), increasing the actuator's inflating pressure causes the STS to open and then stabilise, allowing the actuator to stop extending once equilibrium has been reached. This mechanism prevents excessive suction pressure reduction due to high inflating pressure and avoids unlimited actuator extension. It is worth noting that the classification accuracy of suction flow depends on the pump's suction capability. When a suction cup shares the same pump with an inflating actuator, the inflating pressure reduces the suction pressure, theoretically compromising sensing functionality. However, in our design (Fig. 5), this influence is negligible, as the reduction in suction pressure is minimal. For future designs where sharing the same pump for suction and inflation is necessary, incorporating the inflating pressure into the model by embedding a pressure sensor between the suction cup and the actuator could offer a practical solution.

Force sensing

As the in-air pulling case shows in Fig. 4D, pulling the suction cup can change the suction pressure which makes suction-based force sensing possible. To determine the relation between the pulling force and suction pressure, we extracted all raw data within the pulling period. Figure S5A shows these extracted data for the 600 grit experiment. When the suction cup first generates a firm suction on the surface with zero pulling force, the suction pressure is at its maximum (the bottom left corner). Initially, increasing the pulling force does not cause suction reduction. This is consistent with our observation that the suction cup disc shrank and slipped on the substrate at the beginning due to its elasticity. When the elastic force and the pulling force reaches a new equilibrium, continuously increasing the pulling force begins to reduce the suction pressure obviously. This region can be model-fitted to predict force. Finally, the suction cup breaks off from the substrate. Note that, since we collected the data randomly by hand pulling, the initial contact conditions were very random. This results in a dispersion of the collected data, reducing the accuracy of suction-based force measurement in these conditions. Meanwhile, pulling then releasing the suction cup several times will make the slippage gradually worsen, and the suction disc cannot readily deform back to its original shape. This is the main cause of the drift over time which can be seen from Fig. 4F.

As shown in fig. S5B, the regions suitable for fitting can be fitted with a power function. Experimental data for different roughness surfaces are shown in fig. S5C. Generally, smoother surfaces lead to higher predictable force thanks to a better suction seal. However, the 320 grit surface is not suitable for fitting due to the irregularity caused by the surface roughness. For the rest (400/600/800/1000 grit surfaces), the fitted curves are shown in fig. S5D and their functions are:

$$\begin{aligned} F_{\text{pull}, 400}(p_m) &= -4.03 \times 10^{-4} p_m^{2.724} + 2.444 \\ F_{\text{pull}, 600}(p_m) &= -5.978 \times 10^{-12} p_m^{7.846} + 3.034 \\ F_{\text{pull}, 800}(p_m) &= -5.858 \times 10^{-11} p_m^{7.423} + 3.046 \\ F_{\text{pull}, 1000}(p_m) &= -2.227 \times 10^{-12} p_m^{7.917} + 5.834 \end{aligned} \quad (8)$$

The fitted functions can then be used to predict the pulling force trend and estimate the force value, together with the four classifiers to achieve multimodal perception by the workflow shown in Fig. 4E.

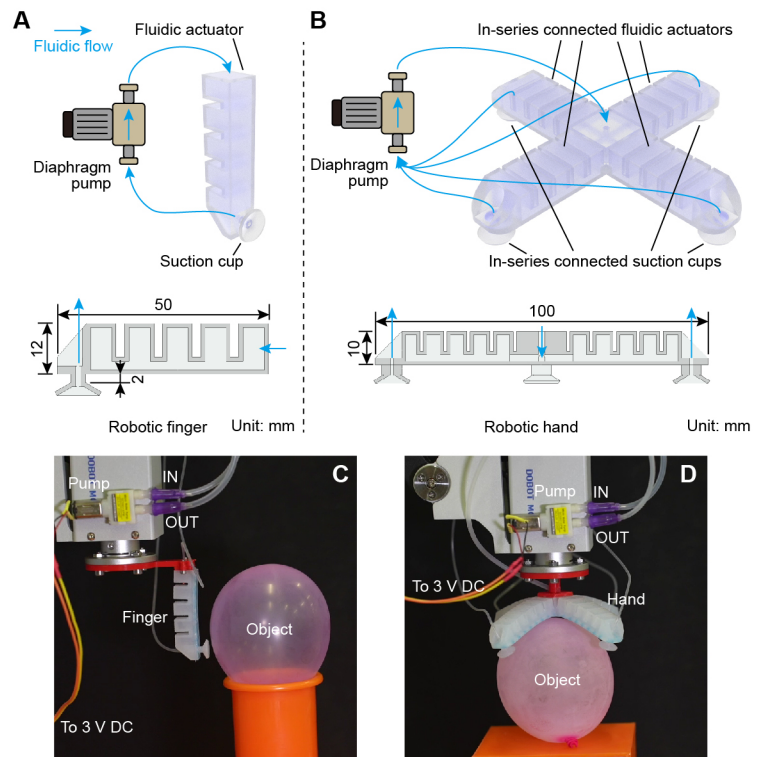


fig. S1. Design and experimental setups of gentle-touch grippers. **(A)** Design of the finger. **(B)** Design of the hand. **(C)** Experimental setup of the finger. **(D)** Experimental setup of the hand.

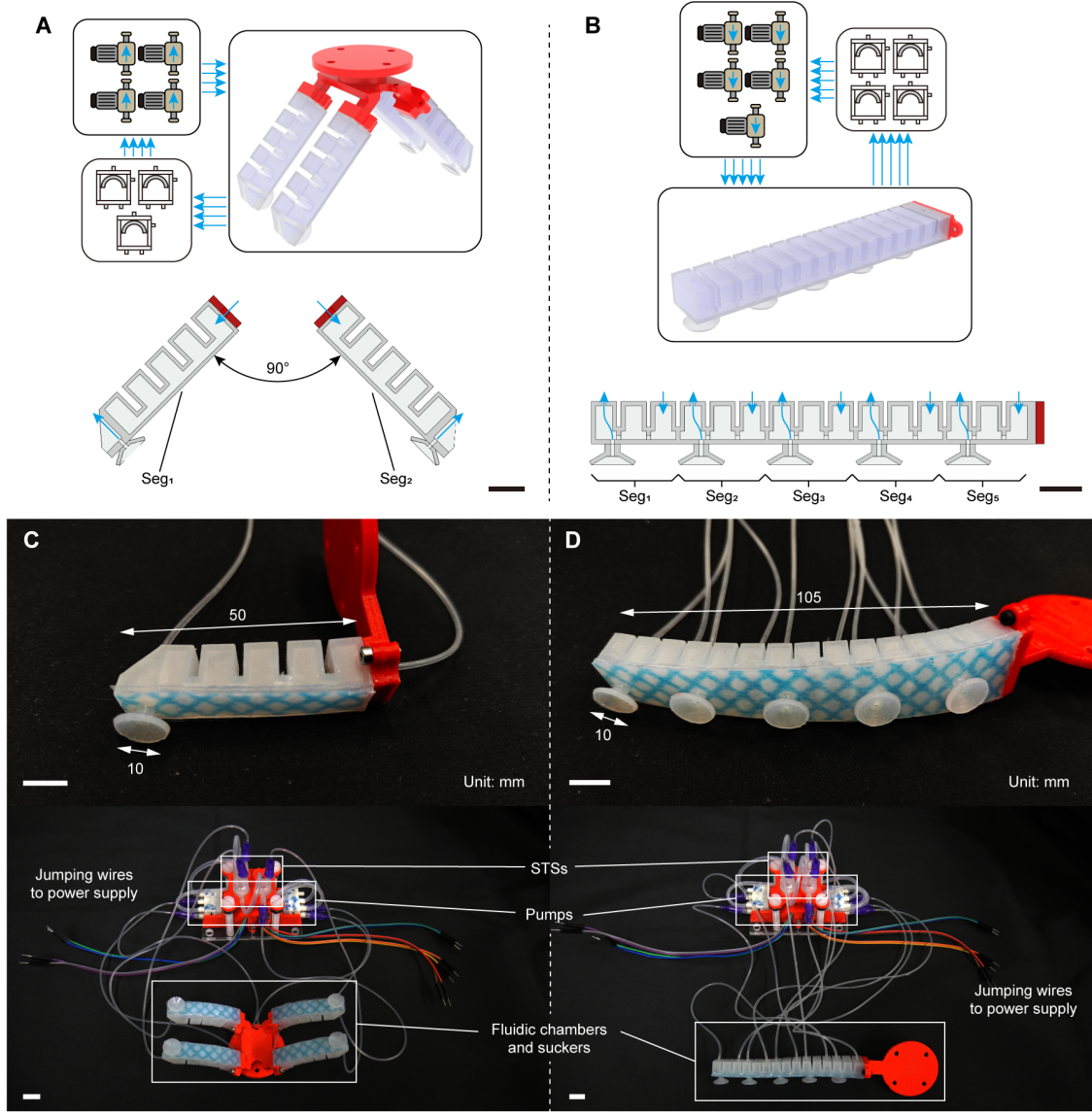


fig. S2. Design and experimental setups of sequential grasping grippers. Scale bars: 10 mm. **(A)** Design of the hand. **(B)** Design of the octopus-like arm. **(C)** Experimental setup of the hand. **(D)** Experimental setup of the arm.

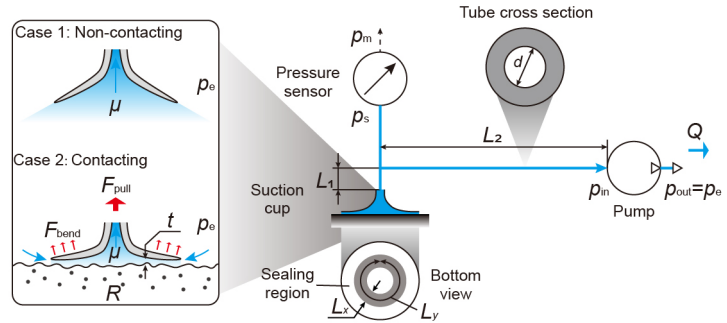


fig. S3. The physical model for perceiving multimodal environmental conditions via suction flow-based method. The pump is powered with constant 3 V.

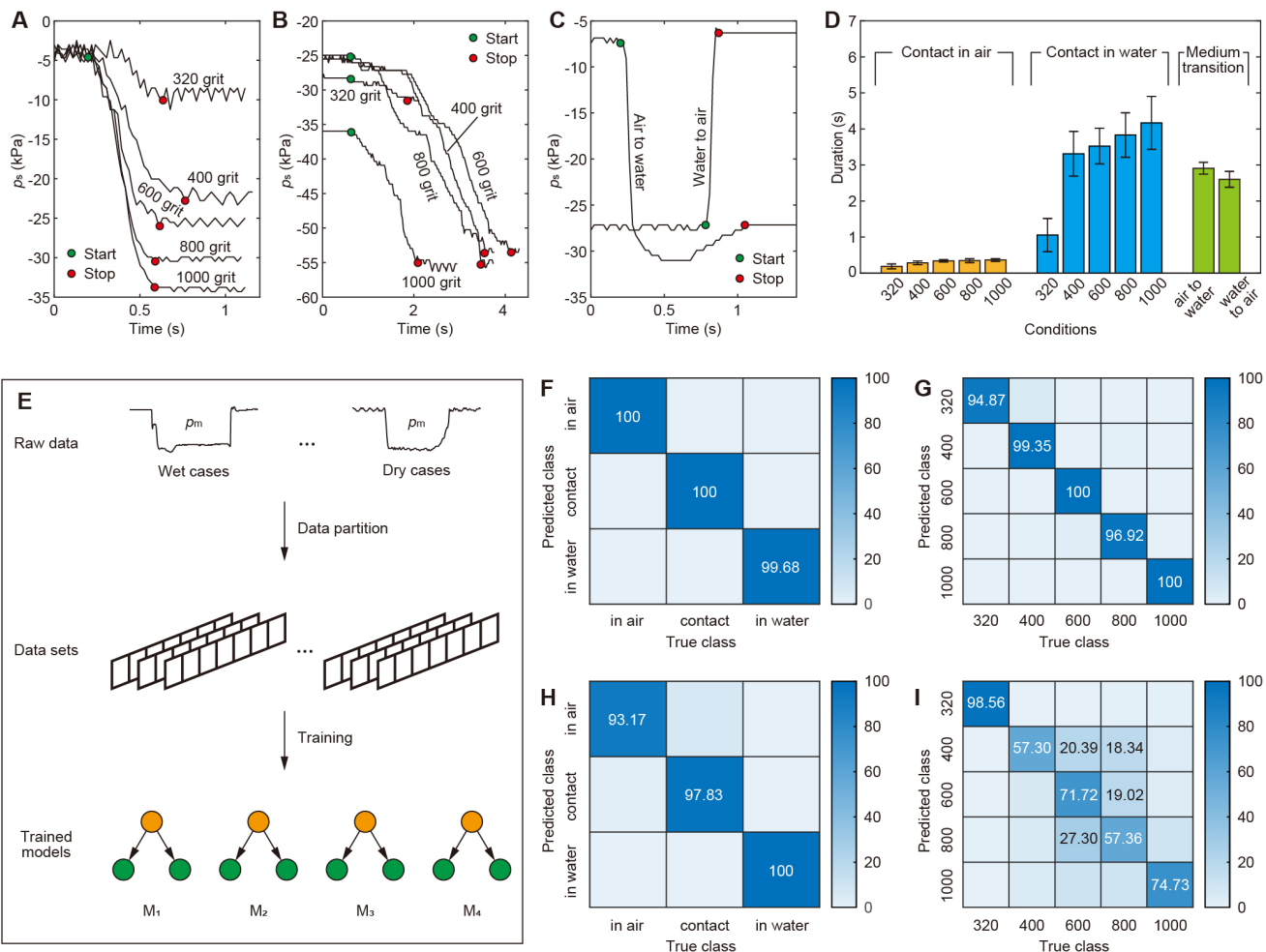


fig. S4. Design and results of the suction-based multimodal perception. **(A) – (C)** Examples of the pressure signal in dry contacting, underwater contacting, and medium transitioning, respectively. **(D)** The event duration of in three conditions. Error bars represent standard deviation ($N = 100$). **(E)** Diagram of processing and training for the suction-based multimodal perception. **(F) – (I)** Classification accuracy of M_1 to M_4 on testing data sets.

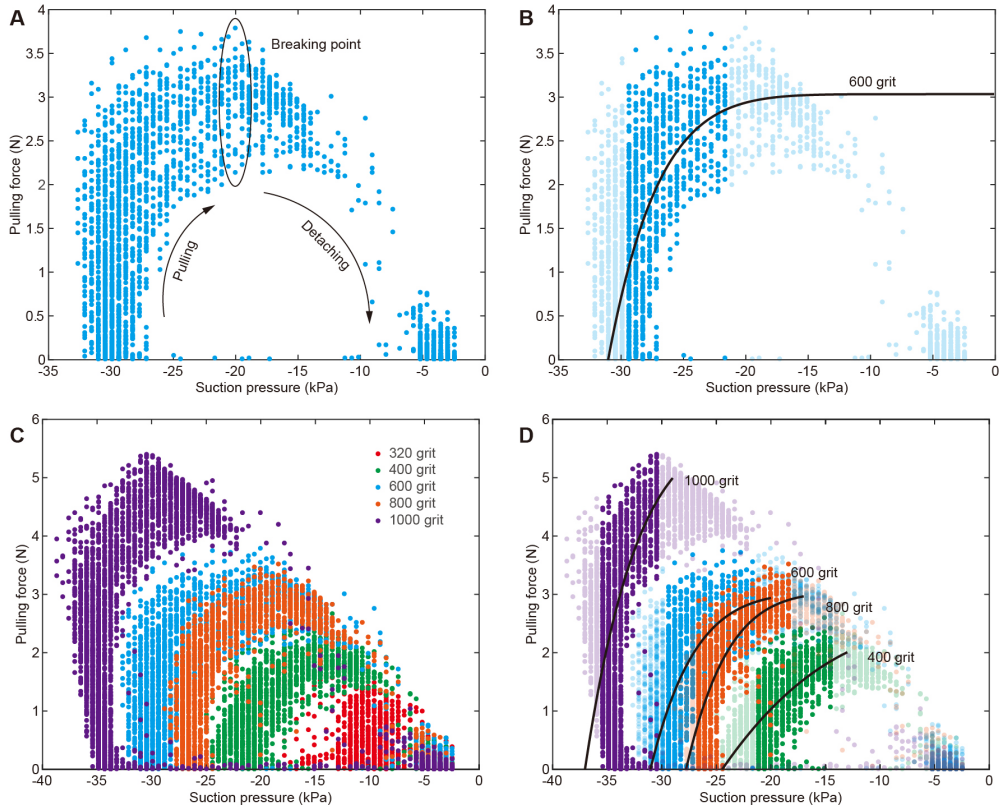


fig. S5. Curve fitting between the pulling force and the suction pressure. **(A)** Collected suction pressure and pulling force data on the 600 grit surface. **(B)** Using the applicable region to fit the force function with a power function, using 600 grit data as an example. The dark blue region indicates the suitable region, while the light blue region indicates the unsuitable region. **(C)** Data collected on five different rough surfaces. **(D)** Fitted power functions on different rough surfaces. 320 grit surface is too rough to provide suitable data for fitting.

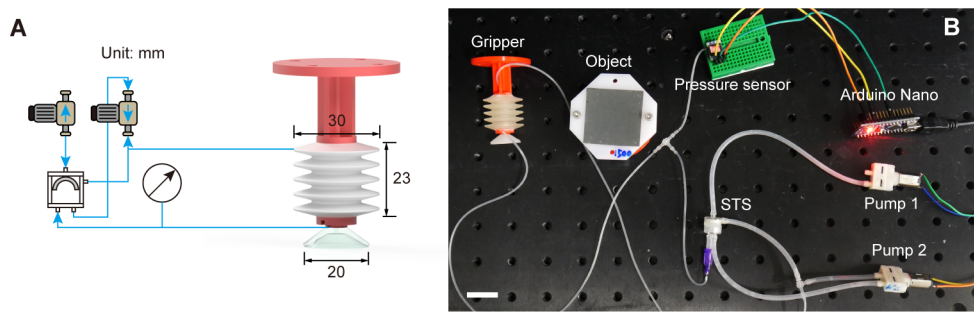


fig. S6. Design and experimental setups of intelligent soft gripper. **(A)** Design of the gripper. **(B)** Experimental setup of the gripper. Scale bar: 20 mm.

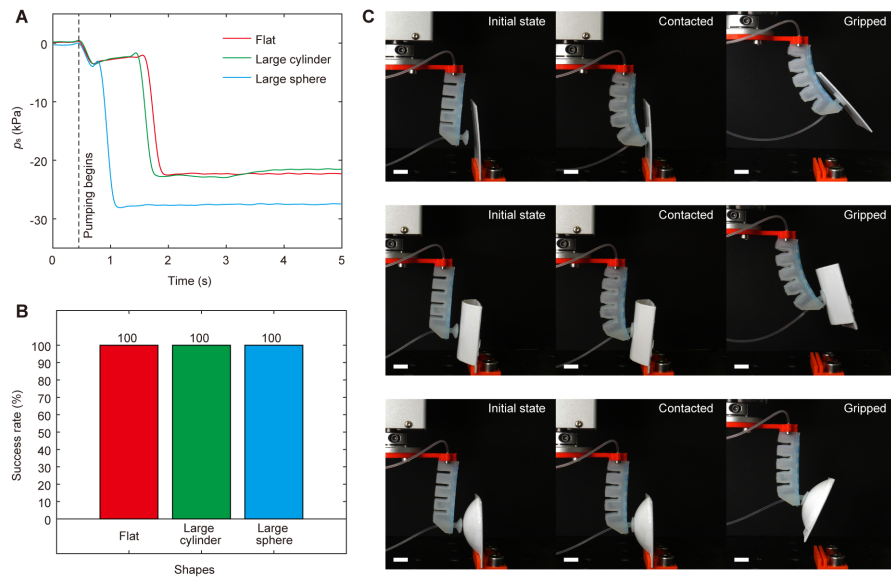


fig. S7. Suction adaptation on different surface shapes. The large cylinder and the large sphere have diameter 50 mm. The suction cup has diameter 10 mm. **(A)** Measured suction pressure during the tests. **(B)** Recorded success rate. Each sample was tested ten times. **(C)** Snapshots of the three conditions. From top to the bottom: the flat plate, the large cylinder and the large sphere. Scale bar: 10 mm.

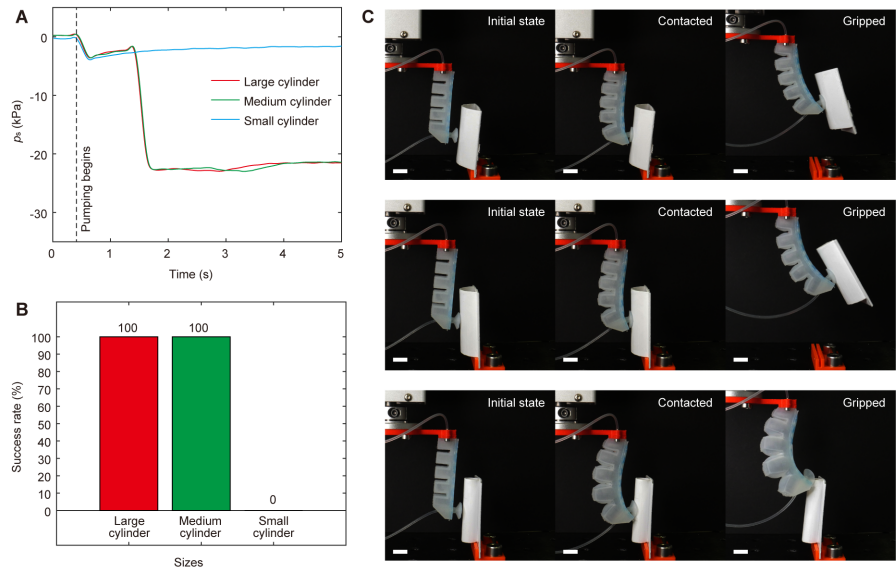


fig. S8. Suction adaptation on different cylinder sizes. The large, medium and small cylinders have diameters 50, 30 and 10 mm, respectively. The suction cup has diameter 10 mm. **(A)** Measured suction pressure during the test. **(B)** Recorded success rate. Each sample was tested ten times. **(C)** Snapshots of the three conditions. From top to the bottom: the larger, medium and small cylinders. Scale bar: 10 mm.

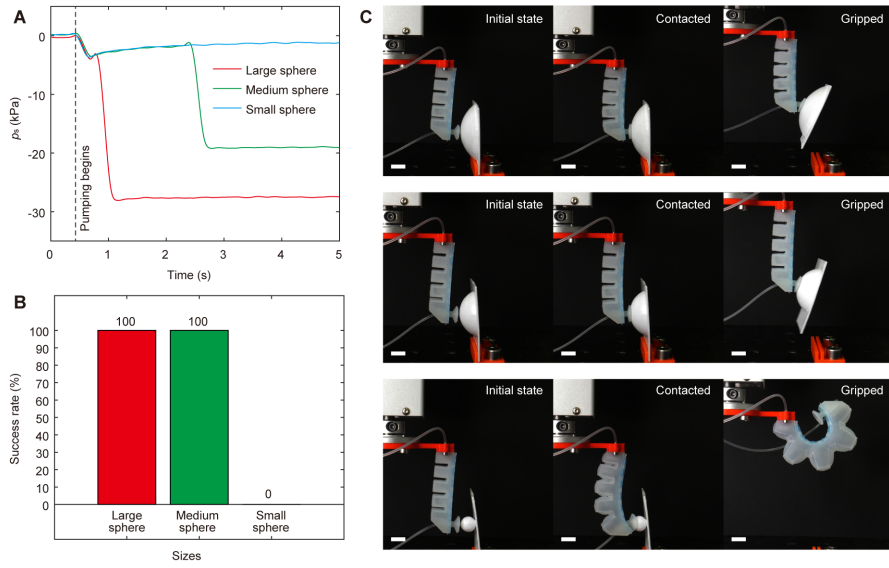


fig. S9. Suction adaptation on different sphere sizes. The large, medium and small spheres have diameters 50, 30 and 10 mm, respectively. The suction cup has diameter 10 mm. **(A)** Measured suction pressure during the test. **(B)** Recorded success rate. Each sample was tested ten times. **(C)** Snapshots of the three conditions. From top to the bottom: the larger, medium and small spheres. Scale bar: 10 mm.

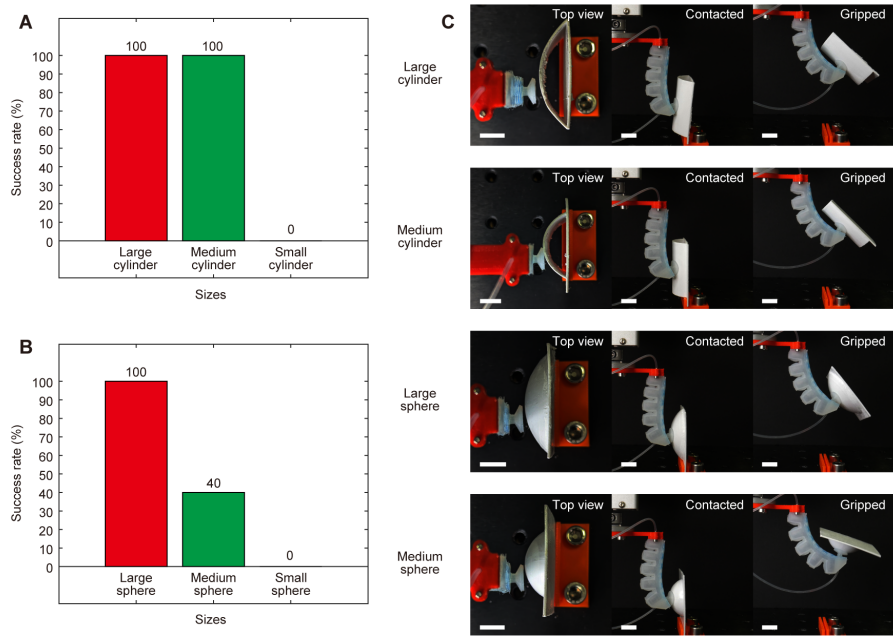


fig. S10. Adaptation when the suction cup is 5 mm misaligned from the geometric centre of the object. The large, medium and small cylinders/spheres have diameter 50, 30 and 10 mm, respectively. The suction cup has diameter 10 mm. **(A)** Measured suction pressure during the test. **(B)** Recorded success rate. Each sample was tested ten times. **(C)** Snapshots of four conditions. Scale bar: 10 mm.

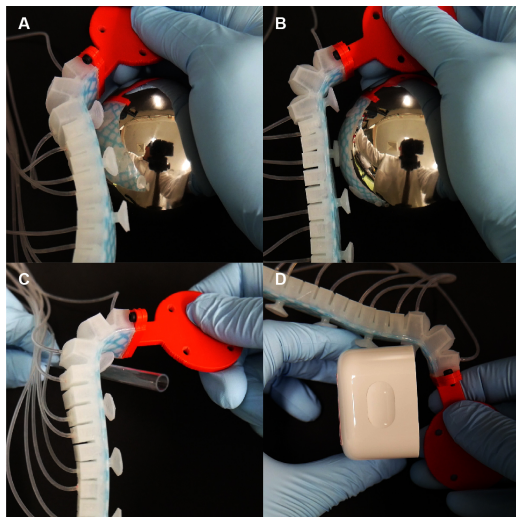


fig. S11. Suction failure in difficult conditions. **(A)** The suction cup is misaligned with the object. **(B)** The suction cup is far away from the object. **(C)** The targeted surface is too small. **(D)** The targeted surface is too sharp.

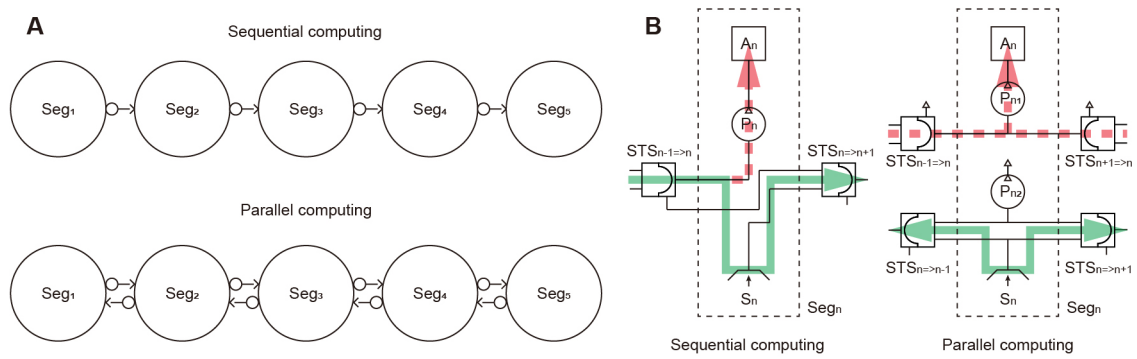


fig. S12. Comparison between the sequential computing and parallel computing. (A) The diagram of the (Seg_1 to Seg_5) sequential computing logic and parallel computing logic. (B) Difference in setups between the sequential computing and parallel computing achieved by the proposed approach.

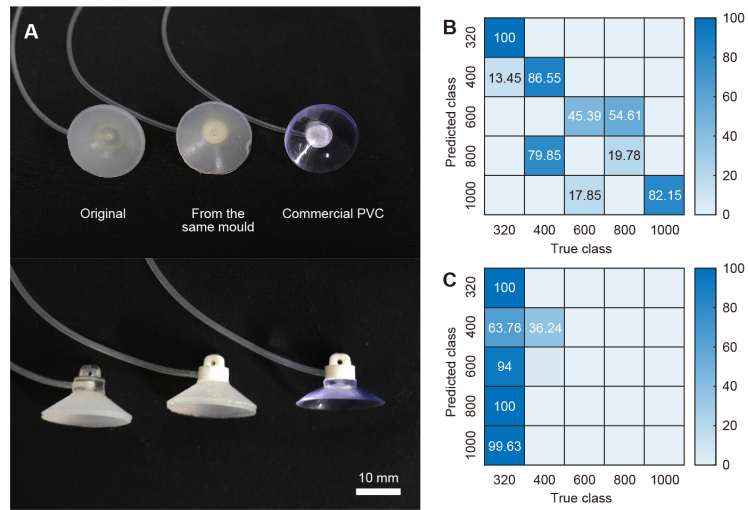


fig. S13. Classification results of different suction cups via the same classifier (M_2). (A) Photos of three suction cups. The original one is used for training M_2 . The middle one was cast from the same moulds as the original sucker. The commercial PVC sucker has a Shore A hardness of 60, making it stiffer than the other two suckers, which have a Shore A hardness of 10. All suckers have the same diameter (20 mm). **(B)** The classification result of the suction cup cast from the same moulds via M_2 . The attach-break test was repeated on the five dry rough surfaces 20 times. **(C)** The classification result of the commercial suction cup via M_2 . The attach-break test was repeated on the five dry rough surfaces 20 times.

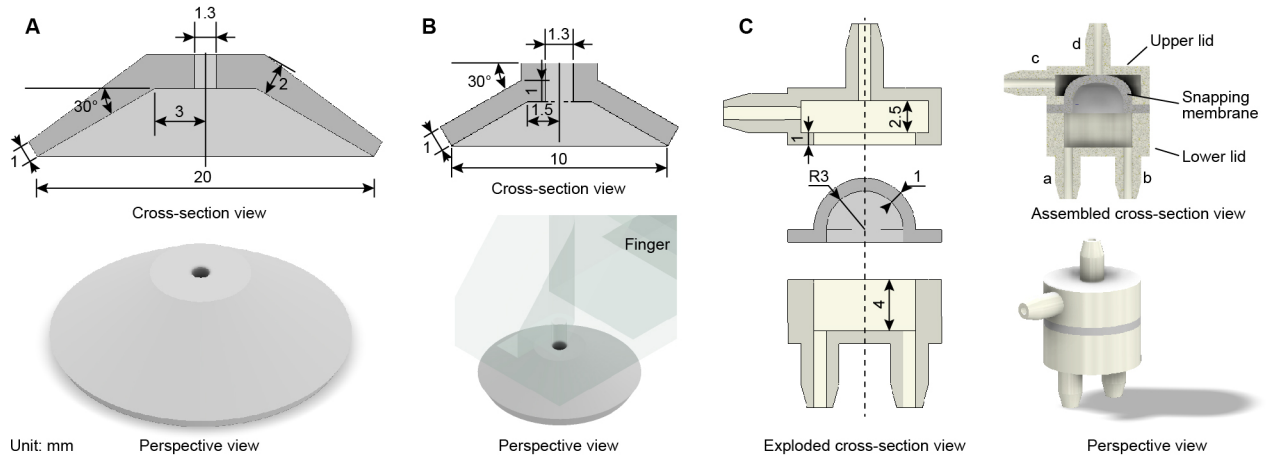


fig. S14. Key dimensions of suction cups and the STS. **(A)** Dimensions of the suction cup for sensing experiments. **(B)** Dimensions of the suction cup embedded in soft robots for semi-autonomous control. **(C)** Dimensions of the larger STS. For the smaller STS shown in Fig. 3D, all the dimensions are reduced to the half. The assembled cross-section view shows that the snapping membrane has a preload on the upper lid, ensuring the safety of the seal.

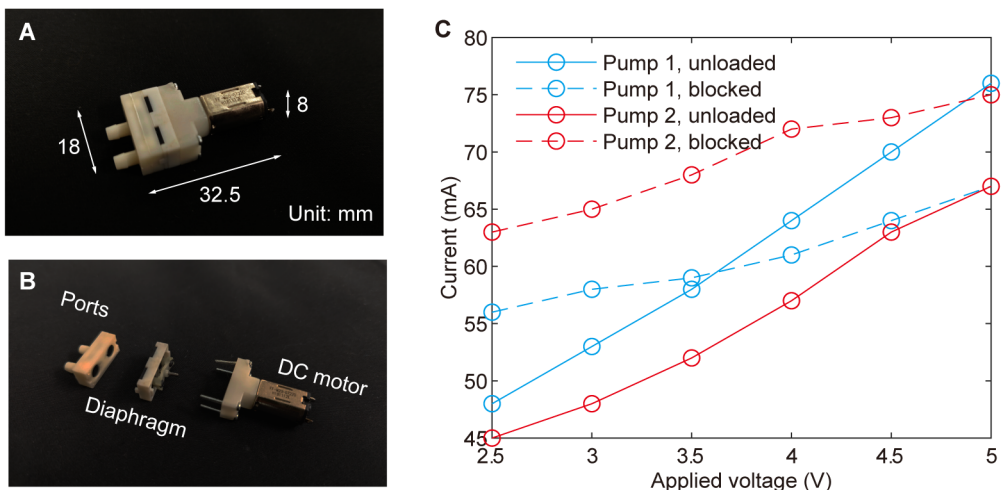


fig. S15. Details of the diaphragm pump. **(A)** The dimensions of the pump. **(B)** The diaphragm structure of the pump. **(C)** The measured current of two pumps under varying voltage supply and loading conditions.

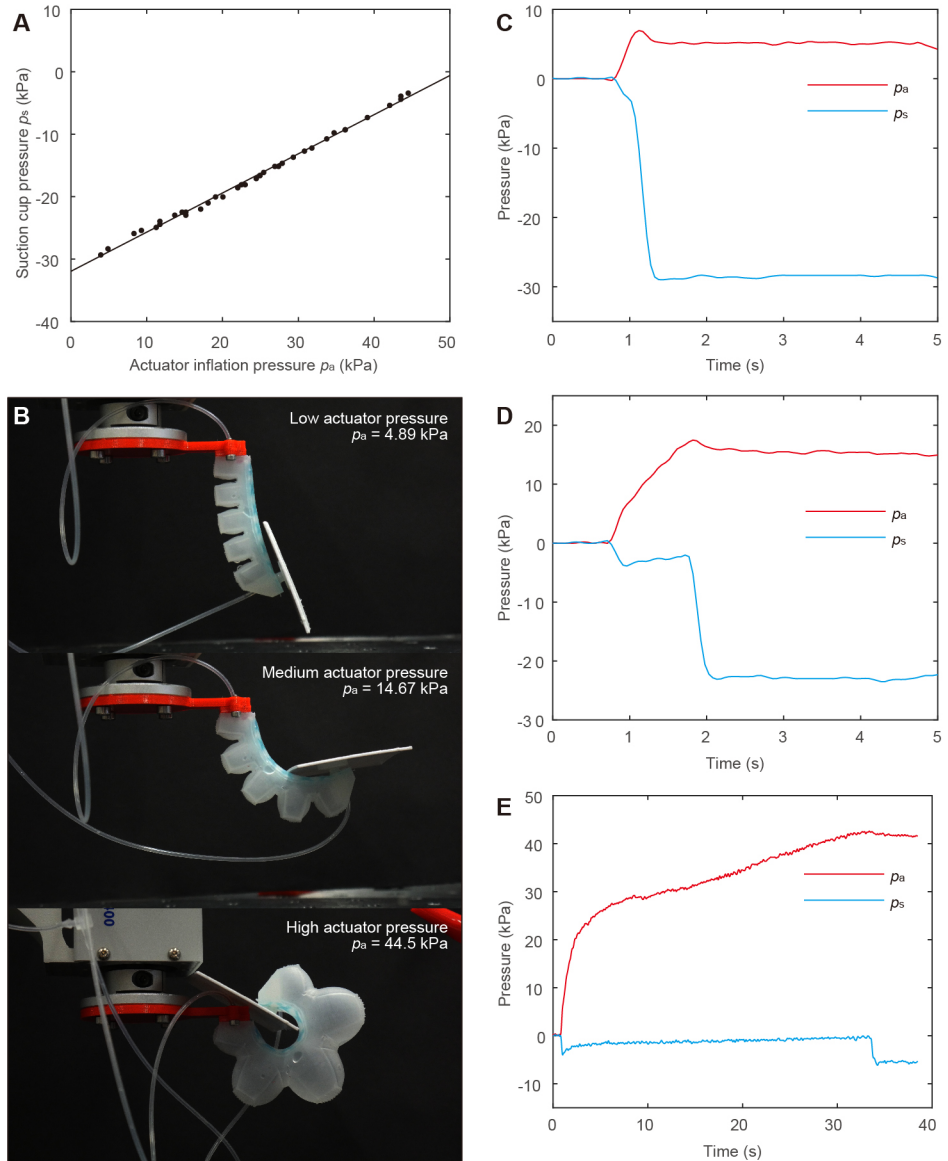


fig. S16. Conditions when the actuator is inflated with different pressure. p_s : suction pressure. p_a : actuator pressure. **(A)** Measured relation of p_s and p_a . **(B)** Photos of the finger grasping a flat plate with low, medium and high actuator pressure. **(C) - (E)** Measured p_s and p_a in the low, medium and high actuator pressure cases, respectively.

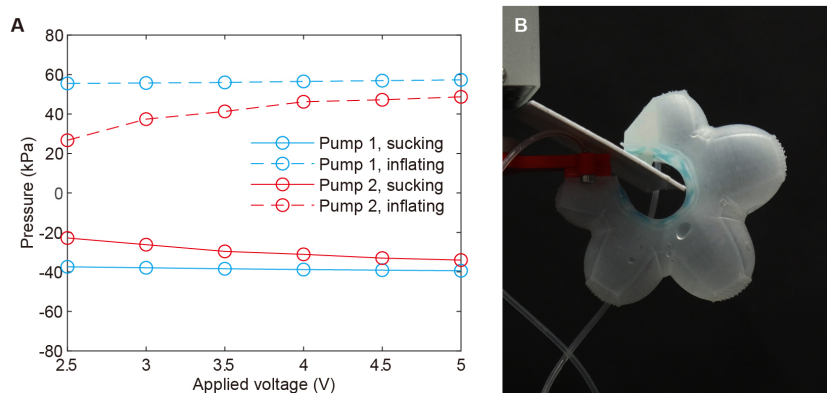


fig. S17. Safety of the system. (A) The measured pump pressure. Two pumps with a large variance due to manufacturing tolerance were selected to test. **(B)** The safety of the actuator under a high inflating pressure (44.5 kPa).

Table S1. Design of the classification tree models

	Model	Data source	Output event	Window size
Suction-based multimodal sensing (Fig. 4)	M ₁	P ₁ – P ₇ , in both wet and dry cases	In air	20 data, 0.44 s
			In air contact	
			Air to water transition	
	M ₂	P ₄ – P ₅ , dry case	320 grit	
			400 grit	
			600 grit	
			800 grit	
			1000 grit	
	M ₃	P ₃ – P ₉ , wet case	In water	140 data, 3.06 s
			In water contact	
			Water to air transition	
	M ₄	P ₄ – P ₆ , wet case	320 grit	
			400 grit	
			600 grit	
			800 grit	
			1000 grit	
Soft gripper with hierarchical intelligence (Fig. 5)	N/A	Whole range	No contact Case 1 Case 2 Case 3 Case 4	140 data, 3.06 s

Table S2. Comparison between the proposed method and previous fluidic-based embodied intelligence approaches

Ref.	Approach	Complexity	Size	Responsive	Programmability	Realisation
(20)	Snapping membranes and kinked tubes	Medium	/	No	Medium	Oscillating the motion of a soft-legged quadruped robot, oscillation
(21)	Floating disc sealing	Medium	~ 10 mm	No	High	Oscillating the motion of the robotic turtle's flippers.
(35)	Origami and kinked tubes	High	~ 25 mm	Yes	High	Enabling a robotic turtle to be reprogrammed to swim
(22)	Membrane buckling and kinked tubes	Low	~ 70 mm	No	Medium	Enabling a beam-climbing robot to do both translational and rotational motion over varied terrain
(23)	Flexible membrane sealing	High	~ 0.5 mm	No	High	Microfluidic-oscillator control of flow in a subordinate fluid circuit
(24)	Snapping membranes and kinked tubes	Medium	~ 20 mm	Yes	Medium	Soft gripper with adjustable grasping force
(25)	Snapping membranes and kinked tubes	Medium	~ 20 mm	Yes	Medium	Soft gripper automatic grasp and release
(37)	Flexible membrane sealing	High	~ 3.25 mm	Yes	High	36 channel fluidic output
(38)	Hysteretic valves	Low	~ 5 mm	No	Low	Sequentially actuated fingers
(26)	Micro check valves	High	~ 0.5 mm	No	Low	Microfluidic control and actuation
(27)	Kinked tubes	Medium	~ 20 mm	Yes	High	Autonomous grasping and release
(36)	Flexible membrane sealing	Medium	~ 10 mm	Yes	Medium	Soft robots preemptively avoiding faults
This work	Suction-triggered seal	Low	~ 6 mm	Yes	Medium	Responsively sequential grasping and oscillating

Note: Each study has its own research focus. Our focus is on the combining the suction-based intelligence with its multimodal sensing property and adhesion property in a simple system.

Table S3. Comparison between digital-controlled hand with suction-based embodied controlled hand

Ref.	Driven method	Sensors	Algorithm	Gripping force	Adaptation	Task complexity	Feature
(28)	Pneumatic-driven	Pressure and attitude sensors	Deep Q-networks	Moderate	High	Three grasping strategies for different objects	Multimodal grasping mode
(47)	Motor-driven	Accelerometers, fingertip pressure sensors	Using three sensory signals to mimic human nerves	Large	High	Can detect force, force disturbance, vibration and slip while grasping	Sensory ability
(48)	Motor-driven	Tactile sensors, vision	Online learning and tracking by a pose graph	Moderate	Medium	Can estimate object's pose and shape	In-hand perception
(49)	Pneumatic-driven	None	None	Gentle	Low	The tradeoff between power grasping strength and precision grasping capabilities for fingers with passive distal segments	Robust precision grasping
(44)	Pneumatic-driven	None	Active control without feedback	Moderate	High	Grasp objects of different sizes, shapes and masses	Shape adaptability and lateral stiffness
(50)	Tendon-and pneumatic-driven	Pressure sensors	Active control without feedback	Moderate	Low	Can quickly grab objects while attached on a flying drone	Collision detection and response
(46)	Thermal-driven	None	Active control without feedback	Moderate	Medium	Can salvage a branch suspended in the water	Self-contained, self-adaptive
(45)	Pneumatic-driven	None	Active control without feedback	Large	High	Can adjust the objects with a range of 0–64.4 mm and an angle range of 0°–140°	Large gripping range
This work	Pneumatic-driven	None	None	Gentle	Medium	Can grasping super brittle objects such as jelly, and gentle sequential grasping on different objects	Simple and low-level autonomy

Legends for Supplementary Movies

Movie S1: Using a simple structure robotic finger to grasp weakly supported objects, including a balloon and a plastic model.

Movie S2: Using a simple structure robotic hand to gently grasp a delicate jelly. In comparison, a regular solid-tip soft robotic hand continuously squeezing the jelly, which is dangerous.

Movie S3: The working principle of the suction-triggered switch (STS). First, we demonstrate the snapping movement of the silicone membrane. Next, we show the blockage and suction-triggered open effect of the STS.

Movie S4: The semi-autonomous grasping behaviour by combining multi-segment soft robots with STSs. First, we demonstrate a four-finger hand gently grasping a plastic model one finger at a time. Next, we show a five-segment arm gently and adaptively encircling two differently shaped objects, similar to a real octopus arm. Finally, we show the integrated intelligent hand grasping different objects.

Movie S5: Suction-based multimodal perception. This movie demonstrates the success of the proposed method for classifying contact, environmental medium and surface roughness, and perceiving pulling force.

Movie S6: The integrated suction adhesion, multimodal perception and embodied intelligence allow the gripper to autonomously execute the extend-suck-retract action without computation from a higher-level computer. Simultaneously, multiple pieces of information about the object, including surface roughness, weight, and surface wetness, can be perceived.

Movie S7: The self-positioning oscillation property of the soft gripper allows it to oscillate around the tip of a grounded round-head pin with a constant flow input. When the upper end of the gripper is moved by the robotic arm, the gripper can automatically adjust its length to ensure the oscillation point maintains its equilibrium position.

Movie S8: The responsive behaviour of the gripper. When a finger gently approaches the suction hole, the gripper retracts; when the finger is removed, the gripper autonomously extends again.